Supporting Information

Zhang et al. 10.1073/pnas.1205945109

SI Materials and Methods.

Benchmarking the EM Energy. In order to use 2D EM images to refine molecular structures, we need a score that measures the similarity between a 3D structure and 2D images. Our score is defined as the negative real-space cross-correlation between a target 2D EM image and the projection of a 3D structure along an estimated orientation angle. In our refinement protocol we refer to this score as the "EM energy." The lower the EM energy, the more similar the model projection is to the 2D target image. During the model refinement, we lower the EM energy to improve the fit between the model projection and the target image by changing the 3D model and optimizing the projection orientation simultaneously; here we test the discrimination and robustness of the EM energy.

To test the reliability of the EM energy in identifying good models close to the target, 488 decoys are generated with C^{α} rmsd in the range of 0.5–30 Å from the target native lysozyme crystal structure (Fig. S1*A*) using torsional-space normal modes (1) with the software package STAND. These decoys are projected along the z axis (with the z axis defined as pointing into the paper). We then generate simulated target EM images by projecting the native lysozyme structure along different orientations; $\theta = 0°$ or 15°, where θ is the altitude angle to the z axis. Different levels of white noise $\eta = 0\sigma$, 1σ, or 20σ (σ is the standard deviation of the pixel values in the image, normalized to 1) are added to target images to mimic experimental images with different signal-to-noise ratios. Modeling this experimental condition is done by normalizing the noise-free projection image using the "*norm*" option in the *proc2d* command in EMAN (2) to a pixel value average of zero and pixel value standard deviation of 1, and then adding different levels of noise using the "*addnoise*" option in *proc2d*. The "*addnoise=level*" option adds a flat-band noise with pixel values in a Gaussian distribution with *level* as the mean and *level/2* as the standard deviation.

Next, the EM energies between the decoy projections and the target EM images are calculated (Fig. S1 *B–F*). Fig. S1*B* shows the case where the target EM image is generated by projecting the native model along the z axis without any noise added ($\theta = 0°$, $\eta = 0\sigma$). In this ideal example, there is no difference in the projection angles between the target model and the decoys. The C^{α} rmsd from the native structure tends to decrease as the EM energy decreases. Although more distant decoys with $8 \sim 20$ Å C^{α} rmsd may share a similar energy value (e.g., −0.8), the EM energy becomes more sensitive in distinguishing models with smaller C^{α} rmsd values. The lowest EM energy also corresponds to the model with the smallest C^{α} rmsd. The observed overall agreement between C^{α} rmsd and EM energy indicates that our EM energy can be used to refine 3D structures against 2D EM images. The funnel-like shape of the plot shows that the EM energy becomes more discriminating as the decoys get closer to the target structure.

In Fig. S1*F*, the target image is projected with $\theta = 15°$. In this case, we test the robustness of the EM energy in selecting good models in the presence of orientation inaccuracy, which is particularly necessary with real data. In addition to the orientation inaccuracy, a noise level of $\eta = 1\sigma$ is added to the target image. This noise level is similar to the level in a typical cryoelectron microscopy (cryo-EM) 2D class average. After taking account of orientation inaccuracies and noise, we find that the funnel-like shape is preserved in the C^{α} rmsd vs. EM energy plot. Due to orientation inaccuracies and noise, the EM energy never achieved an exact match (its value never reaches −1). However, the lowest energy is still able to identify decoys with C^{α} rmsd less than 5 Å from the target structure. This result suggests that it is possible to refine a 3D model against a 2D cryo-EM class average even with a 15° error in the initial estimate of the orientation parameters. In practice, we simultaneously refine the orientation parameters, explicitly minimizing orientation inaccuracy.

However, we do find that with an image noise level of $\eta = 20\sigma$, similar to the noise level in an unaveraged raw cryo-EM image (Fig. S1*D*), the C^{α} rmsd vs. EM energy plot no longer holds a clear funnel-like pattern and cannot be used to refine structures due to the low signal-to-noise ratio.

Generating a Series of Projection Orientations Around the Initial Orientation Ω_{in}. Each orientation is represented by the Euler angle (**Az**, **Alt**, **Phi**) following a ZXZ convention (a rotation of **Az** around the z axis, followed by a rotation of **Alt** around the x axis, and another rotation of **Phi** around the new z axis). For an initial orientation with **Az** $= \alpha$, **Alt** $= \beta$, **Phi** $= \gamma$, the series of projection orientations are generated as follows: (*i*) Set angle varying range to ϵ; (*ii*) set angle varying interval to δϵ; (*iii*) pick **Az** values between $[\alpha - \varepsilon, \alpha + \varepsilon]$ with interval of $\delta\varepsilon$; (*iv*) pick **Alt** values between $[\beta - \epsilon, \beta + \epsilon]$ with interval of $\delta\varepsilon$; (*v*) pick **Phi** values between $[\gamma - \epsilon, \gamma + \epsilon]$ with interval of $\delta\varepsilon$; (*vi*) use all combinations of the **Az**, **Alt**, and **Phi** as the new projection orientation Euler angles.

The initial α, β, and γ are estimated by maximizing the match between the model projection and the target image. The range ε and the interval $\delta\varepsilon$ are set by the user to decide how much and how fine to vary the Euler angle to optimize the projection orientation. Although some of the orientations defined by these Euler angles may overlap, this angular sampling performs sufficiently well for the current application.

1. Levitt M, Sander C, Stern PS (1985) Protein normal-mode dynamics: Trypsin inhibitor, crambin, ribonuclease and lysozyme. *J Mol Biol* 181:423–447.

2. Ludtke SJ, Baldwin PR, Chiu W (1999) EMAN: Semiautomated software for high-resolution single-particle reconstructions. *J Struct Biol* 128:82–97.

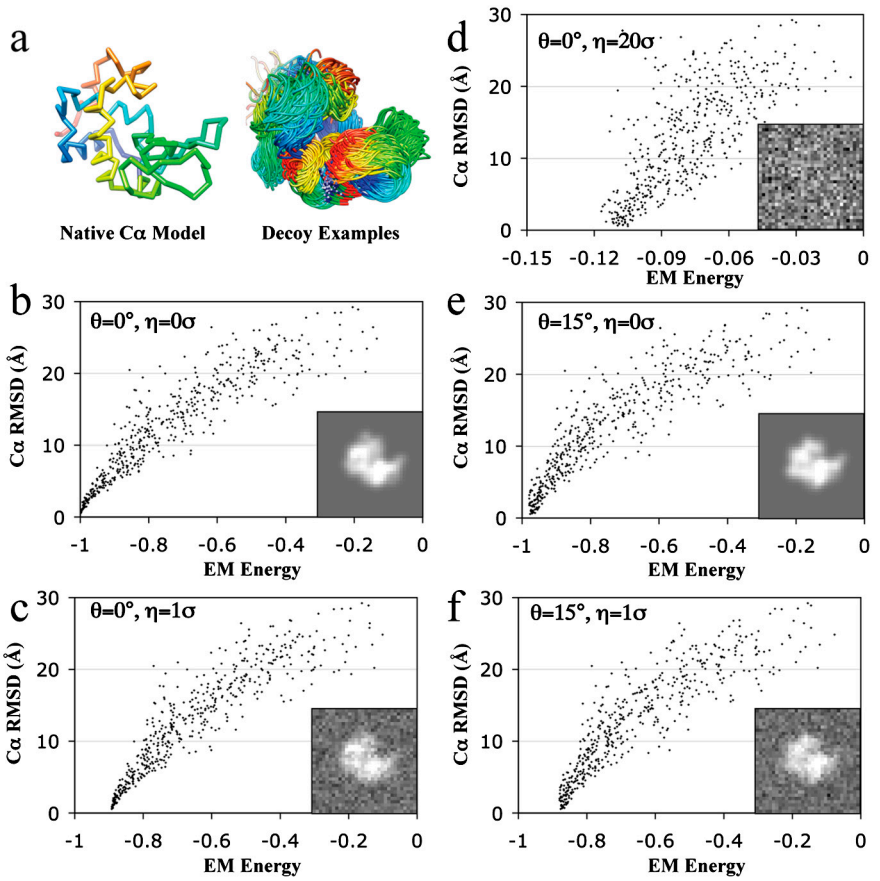

Fig. S1. Using 2D EM images to refine molecular structures. (*A*) C^{α} model of native lysozyme crystal structure (*Left*) with Protein Data Bank (PDB) code: 1LYZ and some of the 488 decoys (*Right*) generated with C^{α} rmsd values that range from 0.5 to 30 Å from the native structure. (*B–F*) C^{α} rmsd vs. EM energy plots for target images with different projection conditions of $[\theta = 0°, \eta = 0\sigma]$, $[\theta = 0°, \eta = 1\sigma]$, $[\theta = 0°, \eta = 20\sigma]$, $[\theta = 15°, \eta = 0\sigma]$ and $[\theta = 15°, \eta = 1\sigma]$, respectively. The insets show the simulated target EM images projected under the relevant conditions from the native C^{α} model in *A*.

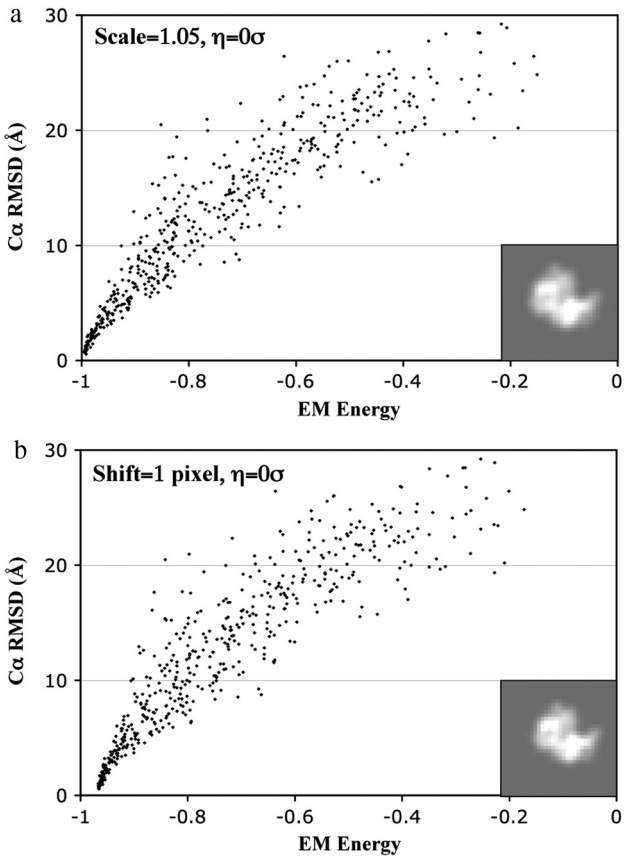

Fig. S2. C^{α} rmsd vs. EM energy plot for target images projected along the *z* axis with no noise added but changed as follows: (*A*) scaled 1.05 times and (*B*) shifted 1 pixel along the *x* axis. The inset in each figure shows the simulated target EM image projected under corresponding conditions from the native lysozyme C^{α} model scaled and shifted accordingly.

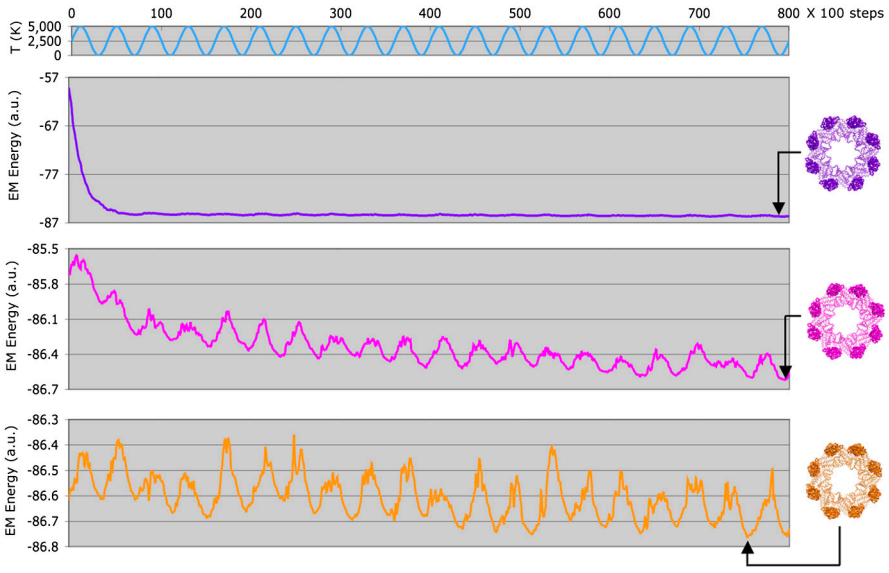

Fig. S3. Temperature-modulated Natural Move Monte Carlo (NM-MC) refinement for three levels of Mm-cpn DOF. The blue curve is the temperature as a function of the steps used in our NM-MC protocol. EM energy change in atomic units is shown as function of the temperature modulated NM-MC steps for level 1 (purple curve), level 2 (magenta curve), and level 3 (orange curve). The black arrows indicate the step with the lowest EM energy for each level; the corresponding refined models are shown on the right. The EM energy is scaled by 100.

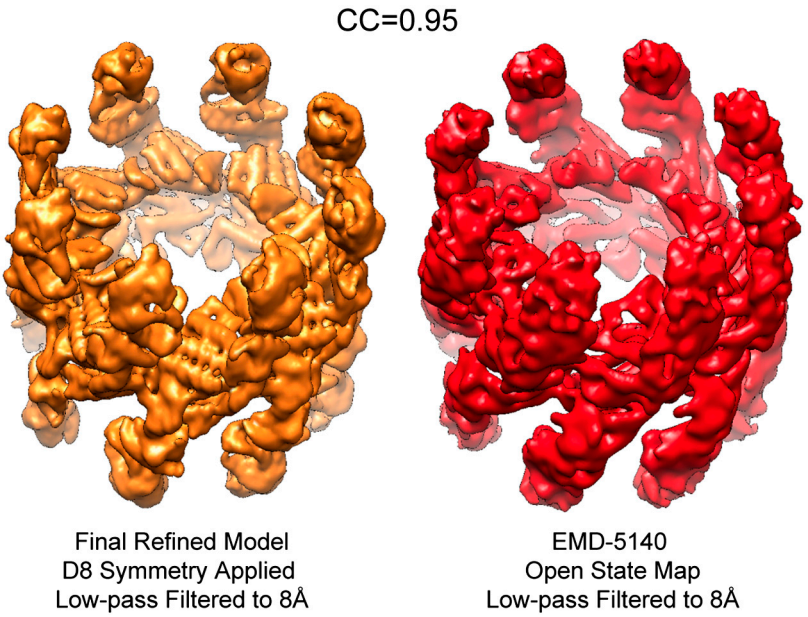

Fig. S4. Final refined model is converted to a density map (orange) at 8 Å resolution with D8 symmetry applied. The open-state map (red, EMD-5140) is denoised to similar resolution 8 Å as the map on the left. Both maps have a cross-correlation value of 0.95.

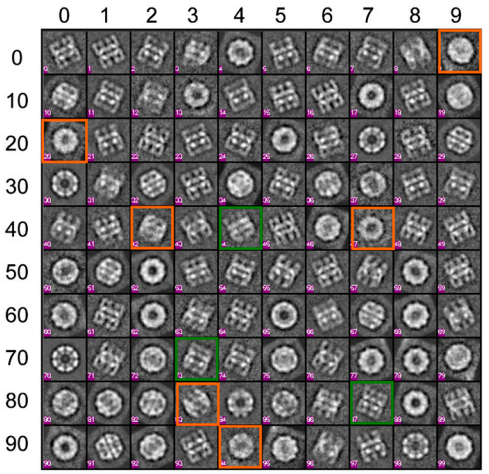

Fig. S5. One hundred 2D class averages are generated from 10,000 cryo-EM raw particle images representing ATP/aluminum fluoride (AlFx) and ATP-free states of the lidless Mm-cpn raw particle conformations. The initial raw particles of these two states had been boxed out of micrographs with box sizes of 192 × 192 pixels and 240 × 240 pixels, respectively. Therefore, the 5,000 ATP/AlFx state of lidless Mm-cpn raw particles were first expanded to a box size of 240 × 240 pixels to match that of the ATP-free state. To expedite the process for both generating the 2D class averages and the subsequent NM-MC refinement, the 10,000 cryo-EM raw particles were then shrunk four times to get an image size of 60 × 60 pixels and a new pixel size of 5.32 $Å^2$. The final 100 2D class averages used for the NM-MC refinement were clipped to a box size of 48 × 48 pixels, and are shown in this figure. Class averages in the orange boxes have low clarity, likely due to misclassified particles in the 2D analysis. Class averages in the green boxes are side views of the open state, which have a slightly lower average center to tip distance (ACTD) (Fig. S7) that is still close to 85 Å. To test the robustness of the refinement procedure, even class averages with low clarity were included in the analysis.

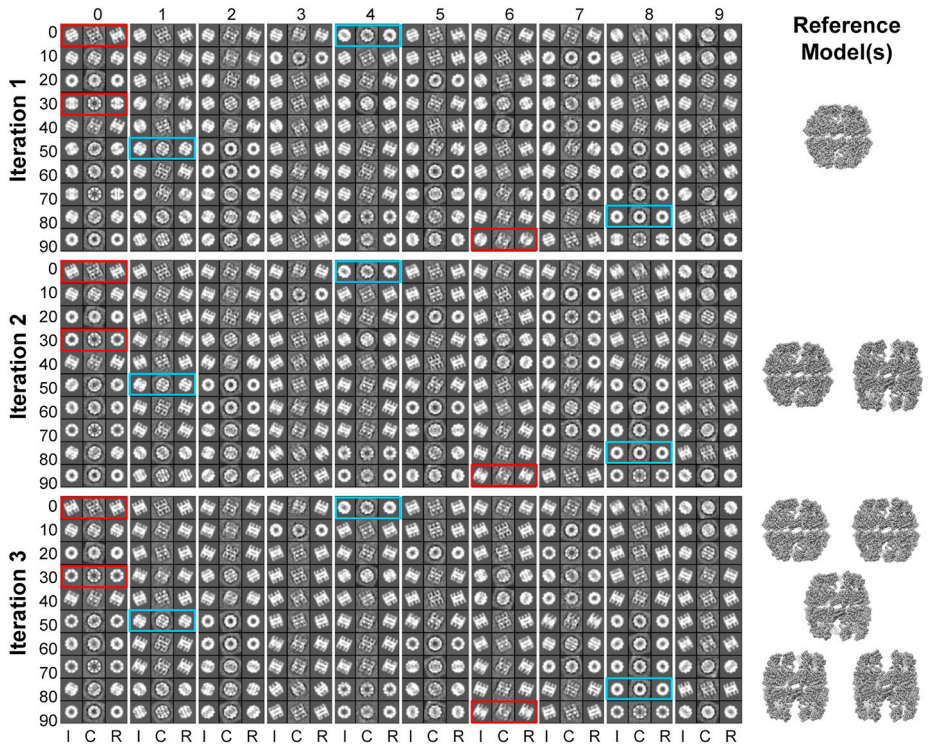

Fig. S6. Three iterations of the NM-MC refinement against the 100 class averages. Column C is the target class average to refine against. Column I is the projection of the initial model along the orientation estimated using the reference model(s) on the right for the current iteration. Column R is the projection of the each of the 100 refined models along a new refined orientation. Six representative refinements for averages #0, #4, #30, #51, #88, #96 are labeled in red (open state) and blue (closed state) boxes. In iteration 1, only the closed-state model is used as a reference to estimate the initial orientation of each of the 100 class averages. This model is then used as the initial model to refine against each of the 100 class averages. In iteration 2, the two averaged models from the two clusters identified in iteration 1 are used to re-estimate the initial orientation of each class average. By using multiple models, this procedure correctly determines orientations that were wrongly estimated during iteration 1. Then each of the 100 class averages is used to refine against its own reference model, which was averaged from the cluster determined from the previous iteration. Then five reference models were averaged from the resulting models from iteration 2 and used to initialize the next iteration. The clustering of the refined models is illustrated in Fig. S7.

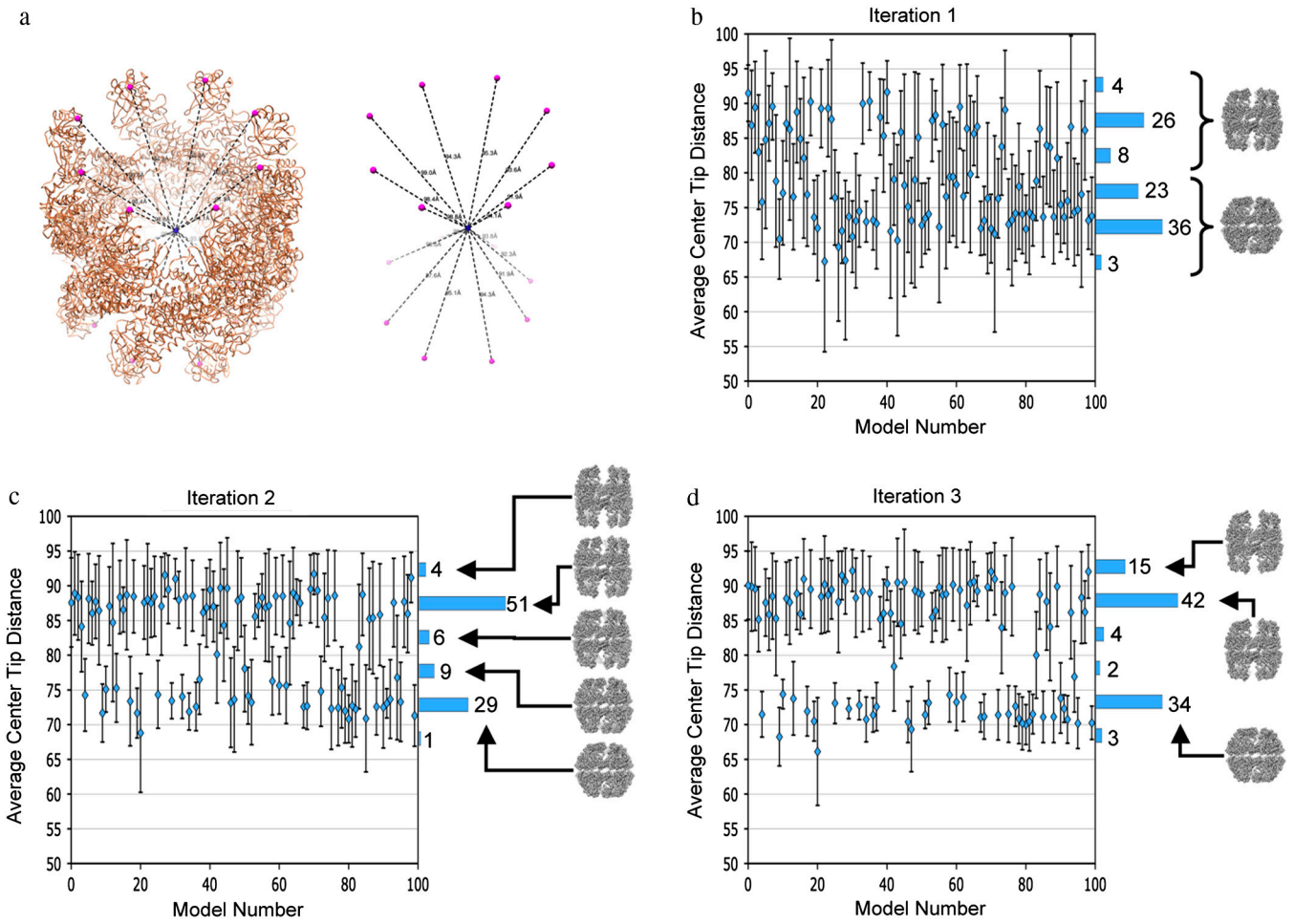

Fig. S7. Clustering of the resulting models from each iteration of NM-MC refinement in Fig. S8 using the ACTD of all the 16 subunits. (*A*) The ACTD can be calculated for each resulting model by measuring the distance between the tip of each lidless Mm-cpn and the center of the chamber. Its value is a measure of the opening of the folding chamber. On average, the ACTD value is about 72 Å for the closed state and 95 Å for a fully extended open state. The standard deviation of the center tip distances of the 16 subunits is a measure of deviation from D8 symmetry. *B–D* show the ACTD values of each of the 100 refined models after each iteration of the NM-MC refinement plotted as blue dots with the error bar representing the standard deviation among the 16 subunits within each model. After three iterations of NM-MC refinement, the standard deviation vs. the ACTD percentage is about 4% for the closed state (ACTD standard deviation of approximately 3 Å) and 6% for the open-state (ACTD standard deviation of approximately 5 Å); this result indicates a more flexible open state that deviates from the D8 symmetry. The histogram on the right of each figure indicates the number of models that fall into the category with the specific ACTD range. For iteration 1, the resulting models are roughly separated by the ACTD value of 80 Å, with $23 + 36 + 3 = 62$ models averaged into state 1 and $4 + 26 + 8 = 38$ models averaged into state 2. These two averaged models are used to initialize the NM-MC refinement for iteration 2 and the resulting refined models are grouped and averaged into five averaged models. These five models are then used to initialize the third iteration and the resulting models fall into three major groups with populations of 15, 42, and 34. Careful examination of the nine 2D class-average projections that produce the models with ACTD values of approximately 65–70 $65 \sim 70$ Å (three models), approximately 75–80 Å (two models), and approximately 80–85 Å (four models) shows that six of the nine 2D class averages have low quality (orange boxes in Fig. S5) and three of the nine capture open state, which has an ACTD slightly less than 85 Å (green boxes in Fig. S5). Further analysis of the three major populations with ATCD $90 \sim 95$ Å (15 models), ACTD $85 \sim 90$ Å (42 models), and ACTD $70 \sim 75$ Å (34 models) show the first two groups are very similar. The C^{α} rmsd between the averaged models from the first two populations is less than 3 Å, but it is 12 and 10 Å between the averaged models of the first and third major groups and the second and third major groups, respectively. Therefore, the first two groups ($15 + 42 = 57$ models) are combined into one single state, and the 34 models with ACTD values of $70 \sim 75$ Å are assigned to another state. Averaging of the models within each cluster is done by: (*i*) aligning the models to minimize their C^{α} rmsd; *ii*) averaging their Cartesian coordinates.

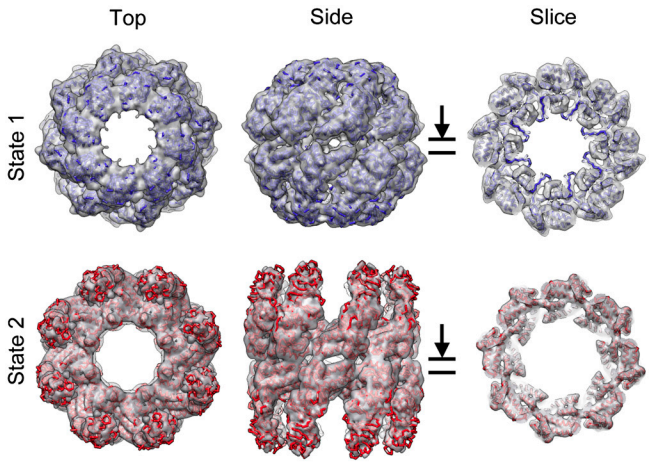

Fig. S8. Re-refined density maps after the EMAN *multi-refine* step reveal secondary structure. The previously published models, which were built from lidless Mm-cpn maps reconstructed from larger numbers of homogeneous raw particles, are fitted into our re-refined density maps from the heterogeneous dataset. The slice view of the equatorial domain shows nice agreement between the sausage-like helices density with the α-helices in the model. To push for the resolution, the unshrunk 10,000 raw particle images were used with a pixel size of 1.33 Å. Because of the limited number of particle images, D8 symmetry was imposed during the reconstruction. The short black bars indicate the location of the slice, and the black arrows indicate the viewing angle of the slice view.

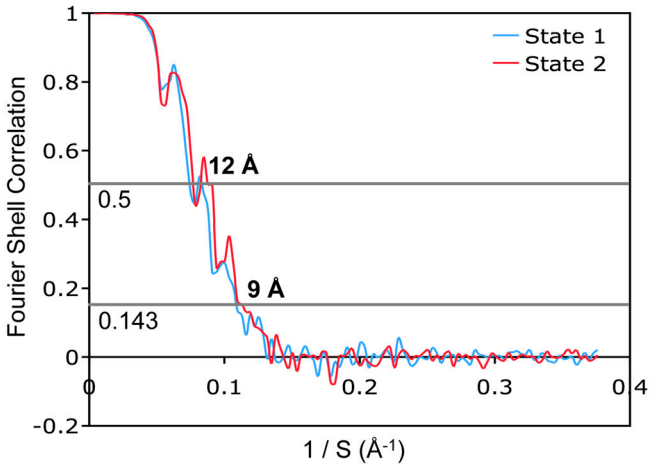

Fig. S9. Final Fourier shell correlation allows us to assess the resolution of the re-refined maps of states 1 and 2.

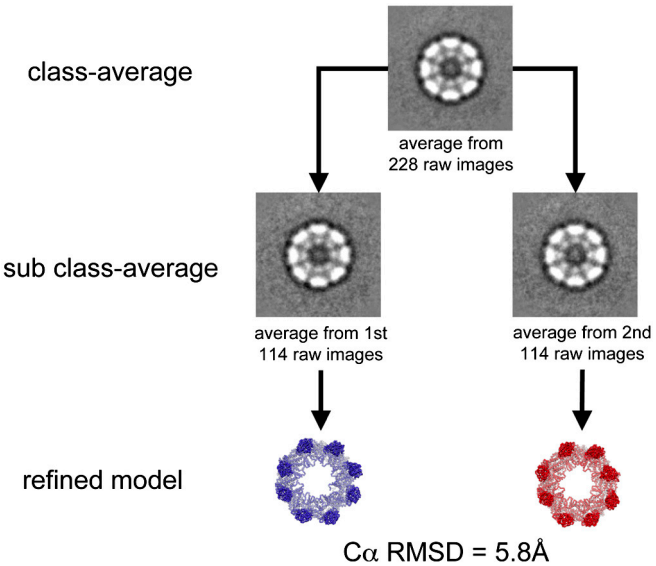

Fig. S10. Cross-validating the refinement result. A total of 228 raw images of lidless *Methonococcus maripaludis chaperonin* (Mm-cpn) were divided into two groups to generate two subclass averages. The same refinement protocol used for the original class average was applied to each subclass average using the closed-state lidless Mm-cpn as an initial model. The refined models have a C^{α} rmsd value of 5.8 Å.

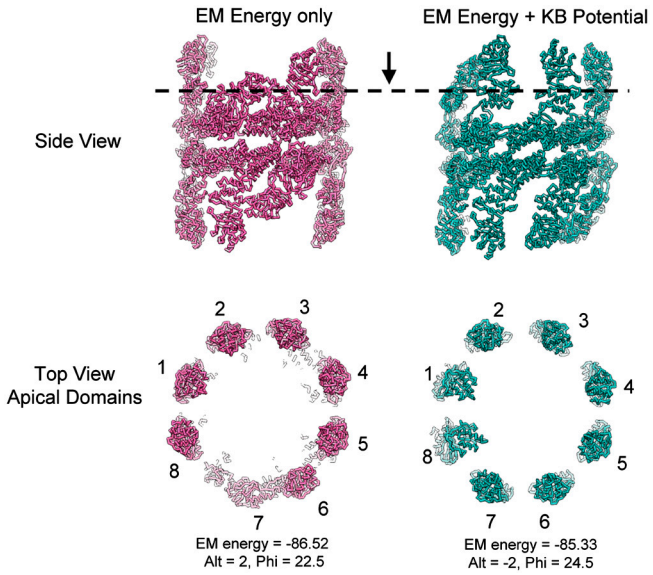

Fig. S11. Refinement result by skipping level 1 and directly using level 2 degrees of freedom (DOF). Side view and top view for the refined model by the EM energy only (magenta) or by both the EM energy and the knowledge-based potential (cyan). The viewing angle and clip plane is indicated by the black dashed line and arrow.

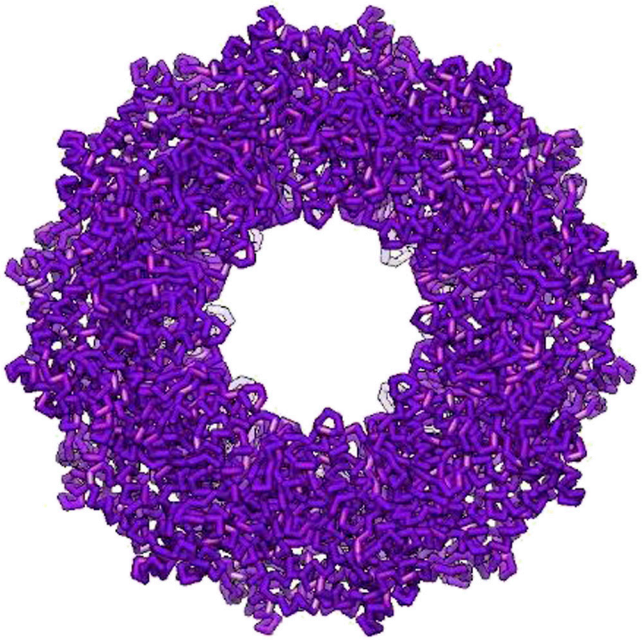

Movie S1. First 10,000 steps of the temperature modulated NM-MC refinement of Mm-cpn at level 1 from the closed state to the open state. Models are shown for every 100 steps.

Movie S1 (MOV)

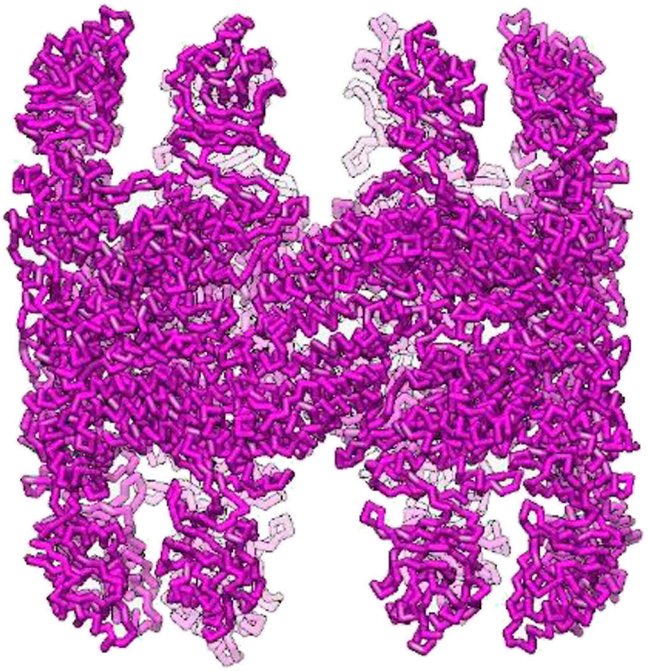

Movie S2. First 10,000 steps of the temperature modulated NM-MC refinement of Mm-cpn at level 2 from the refined model of level 1. Models are shown for every 100 steps.

Movie S2 (MOV)

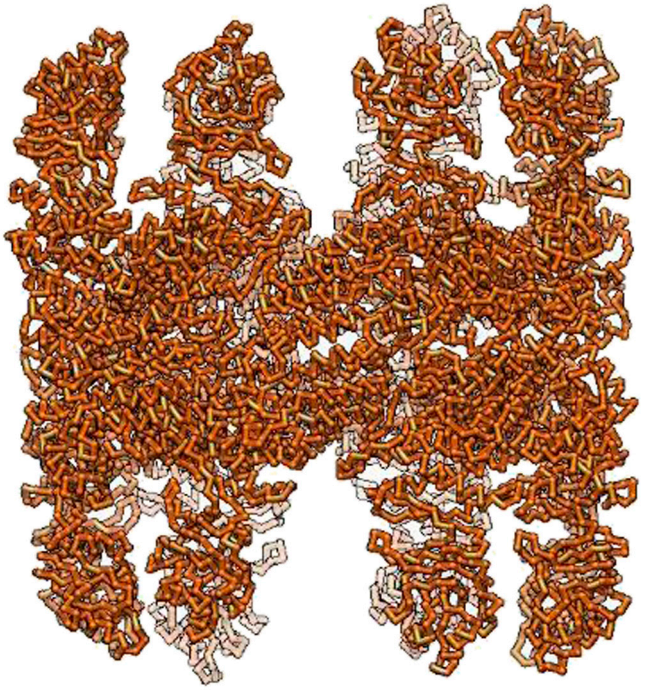

Movie S3. First 10,000 steps of the temperature modulated NM-MC refinement of Mm-cpn at level 3 from the refined model of level 2. Models are shown for every 100 steps.

Movie S3 (MOV)